Periodic Activation Functions for Enhanced Subsurface Defect Segmentation in Infrared Thermography

by Mohammed Salah*, Davor Svetinovic**, and Yusra Abdulrahman***

* Khalifa *University*, Department of Aerospace Engineering, Abu Dhabi, United Arab Emirates
100058291@ku.ac.ae
** Khalifa *University*, Department of Computer Science, Abu Dhabi, United Arab Emirates
davor.svetinovic@ku.ac.ae
*** Khalifa *University*, Department of Aerospace Engineering, Abu Dhabi, United Arab Emirates
yusra.abdulrahman@ku.ac.ae

Abstract

Deep learning-based infrared thermography (IRT) has garnered significant attention in non-destructive testing (NDT) techniques, enabling automatic detection of subsurface defects in industrial components. While most research focuses on improving network architectures, the impact of activation functions is merely explored. For instance, traditional activations struggle to capture fine spatial and temporal features in thermographic representations. Hence, this work proposes leveraging periodic activation functions to enhance implicit neural representations for learning-based defect analysis. Evaluated on the Université Laval IRT-PVC segmentation dataset, the proposed approach improves segmentation accuracies by 7% compared to traditional activation functions, such as ReLU.

Keywords: Infrared thermography, Non-Destructive Testing, Activation Functions, Deep Learning, Defect Segmentation

1. Introduction

The increasing demand for rigorous quality control in the aerospace industry has driven the adoption of advanced non-destructive evaluation (NDE) techniques in aerospace manufacturing [1, 2]. Consequently, a wide spectrum of NDE technologies, including ultrasonic testing, radiography, and infrared thermography (IRT), have been developed to detect hidden anomalies and subsurface defects in aerospace components and assess their structural integrity. Among these technologies, IRT stands out and is valued for its fast-scanning speed, low cost, and non-contact nature [3]. These advantages demonstrated the application of IRT to detect subsurface defects in PVCs [4, 5], composites [6, 7], PLA [8, 9], and concrete structures [10, 11].

Advancements in artificial intelligence (AI) have significantly improved the reliability and accuracy of infrared thermography for defect detection. The most prevalent state-of-the-art IRT approaches involve compressing IRT sequences to thermographic representations, such as principal component analysis (PCA) [12, 13] and Thermographic Signal Reconstruction (TSR) [14, 15], before feeding them into AI models. Extensive research has explored various IRT network architectures for defect detection, segmentation, and depth estimation. However, the impact of network activation functions on defect characterization accuracy remains unexplored, despite their critical role in influencing model performance.

Motivated by the above, this work proposes the IRT-Sinusoidal Representation Network (IRT-SIREN U-Net), a modified U-Net architecture that employs periodic activation functions to enhance implicit neural representations for learning-based IRT defect analysis. Additionally, the study quantifies the impact of different activation functions on the performance of IRT defect segmentation networks. The proposed method is tested on the Université Laval IRT-PVC segmentation dataset and the results show that IRT-SIREN U-Net improves segmentation accuracies by 7% compared to its ReLU counterpart.

1.1. Related Work

IRT has established itself as a key NDT technique for detecting hidden subsurface defects in a range of industrial components. In addition, IRT has recently witnessed the adoption of AI methodologies in IRT setups to further enhance its reliability and detection accuracy. These advancements saw the applications of IRT grow rapidly in aerospace [16] and construction [17] industries, and in inspection of artworks [18]. This growing demand for IRT led to a series of investigations on neural network architectures, triggering the emergence of advanced learning-based IRT defect detection models. To illustrate, Tong et al. [19] and Lema et al. [4] fine-tuned Faster R-CNN and Yolov5 networks for IRT defect detection

applications, respectively. In addition, other network architectures have been proposed such as ConvLSTM [20] for enhanced IRT defect detection.

Similarly, a series of network architectures have been proposed for IRT defect segmentation. Fang et al. [21] experimentally studied state-of-the-art segmentation network architectures for subsurface defect segmentation, such as U-Net and ResNet. In addition, an attention U-Net network was proposed for improved defect segmentation compared to traditional U-Net [22]. These networks employ spatial filters with no regard of the inherent temporal features in thermographic sequences. Thus, 3D-CNNs were proposed to account for the temporal dimension for enhanced segmentation of subsurface defects in industrial components [6]. Still, the developed networks are completely convolutional and the performance of CNNs is limited by the receptive field of the convolutional layers. Therefore, attention mechanisms have been incorporated in IRT defect segmentation networks to address the drawback of the limited receptive field of CNNs and capture long range dependencies in thermographic data [23].

The aforementioned approaches utilize thermography dimensionality reduction techniques to generate thermographic representations as inputs to deep neural networks, while optimizing the network architectures for improved defect characterization accuracies. The most prevalent thermography dimensionality reduction techniques include thermal signal reconstruction (TSR) [14, 15], pulse phase thermography (PPT) [24, 25], and principal component analysis [12, 13]. However, the effect of activation functions in shaping the learning dynamics of IRT networks is unexplored. To address this gap, this work introduces the IRT-SIREN U-Net, a modified IRT U-Net that leverages periodic activation functions to enhance implicit neural representations for defect segmentation. The proposed method also provides a comparative analysis of standard and periodic activations, offering new insights into their impact on segmentation performance.

1.2. Structure of The Article

The rest of the article is structured as follows. Section 2 provides necessary preliminaries for IRT-SIREN U-Net methodology. Section 3 outlines the proposed IRT-SIREN U-Net. Section 4 presents experimental validations of the IRT-SIREN U-Net tested on the IRT-PVC dataset. Finally, section 5 presents conclusions, findings, and future aspects of the proposed work.

2. Preliminaries

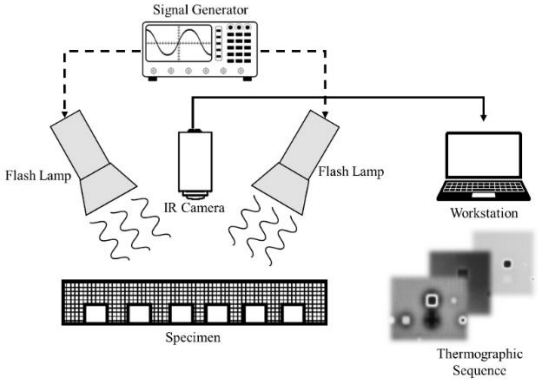

Fig. 1:*Typical IRT setup involving flash lamps and an IR camera. In the presence of defects, heat tends to be trapped, generating an abnormal thermal distribution on the surface of the specimen and recorded by the IR camera for IRT inspection.*

2.1. Infrared Thermography and IRT-PVC Dataset

A typical IRT setup is shown in Fig. 1. IRT involves a halogen lamp stimulating the target specimen with a controlled heat input [2]. If the specimen is sound, all pixels of the IR camera generate similar thermal profiles. If defects are present, heat tends to be trapped, and an abnormal thermal profile is generated on the surface of the specimen and is captured by the IR camera for further analysis.

Several IRT datasets following the general IRT setup are publicly available. In this work, the IRT-SIREN U-Net is evaluated on the IRT-PVC dataset [4, 5]. The dataset comprises 38 inspection sequences of 3D-printed PVC samples with back-drilled holes at depths ranging between 0 and 2.5 mm at increments of 0.5 mm. Each depth increment is designated as a defect class and each inspection sequence $S_i = \{I_k\}_{k=1}^{N_t}$ is a 3D matrix of shape (N_t, N_Y, N_x) with I_k thermograms, where $k = 1, 2, ..., N_t$ is the image timestamp, i represents the sample index, N_Y is the image height, and N_x is its width. $\boldsymbol{S_i}$ is reshaped to $(N_t, N_Y \times N_x)$ by a raster-like operation and standardized by:

$$\widehat{S_i} = \frac{S_i - \mu_k}{\sigma_k},$$

where,

$$\mu_k = \frac{1}{N_t}\sum_{k=1}^{N_t} S_k,$$

$$\sigma_k^2 = \frac{1}{N_t - 1}\sum_{k=1}^{N_t} (S_k - \mu_k)^2,$$

and $\widehat{S_i} = \{S_n\}_{n=1}^{N_y \times N_x}$ is the standardized pixel-wise thermal response.

2.2. Infrared Thermography Representations

Developing IRT networks that process the entire inspection sequence introduces significant computational and memory demands. Instead, the thermal sequences are compressed to PCA and TSR representations, which capture the important information in thermographic signals with reduced dimensionality. For instance, the PCA representation enhances defect clarity, while TSR models the temporal evolution of the pixel responses.

To generate PCA representation, singular value decomposition (SVD) is applied by

$$\hat{S}_i = \mathcal{U}\Gamma V^T,$$

where $\mathcal{U}$ is the set of orthogonal functions representing spatial differences within the input pixel responses, Γ comprises singular eigenvalues, and matrix V contains the principal components. Hence, the PCA images are formulated by

$$P_k = \hat{S}_i v_k,$$

where V_k is the K^{th} eigenvector in V. Note that only the first 5-10 principal components are utilized for creating the PCA images, $P = [P_1, P_2, \ldots, P_J]$ as an input representation for IRT networks.

On the other hand, TSR images are generated by logarithmic n-degree polynomial fitting on the pixel's time responses as

$$\ln(\Delta T) = a_0 + a_1 \ln(t) + a_2 \ln(t)^2 + a_3 \ln(t)^3 + a_4 \ln(t)^4 + a_5 \ln(t)^5,$$

where a_n are the polynomial coefficients, ΔT is the temperature difference, and t is time. It is worth mentioning that in our work a 4-degree polynomial is utilized for creating the TSR representation and the polynomial each coefficient is utilized as a channel for the TSR images. Collectively, a 10 channel PCA image $\boldsymbol{P}$ and 5 channel TSR image $\mathbf{T}$ are generated from each inspection sequence and is utilized as input to IRT-SIREN U-Net.

3. Methodology

3.1. IRT-SIREN U-Net

The architecture of the IRT-SIREN U-Net is shown in Fig. 2. Conventional IRT U-Net architectures utilize the standard activation function ReLU. While these activations demonstrated effectiveness in various computer vision domains including IRT, these non-periodic activations often limit the network's ability to capture high-frequency signal variations and subtle defect patterns inherent in thermographic data. As shown in Fig. 2d, these traditional networks follow a standard *k*×*k* convolution → activation → normalization pipeline within each encoder and decoder block.

In contrast, the proposed *IRT-SIREN U-Net* introduces periodic activation functions into the U-Net structure to improve the network's expressiveness and ability to represent complex signal variations. Fig. 2c highlights this architectural difference, where each block integrates a sinusoidal activation between the convolution and normalization layers. The network preserves the overall U-Net structure, which comprises of a convolutional encoder, bottleneck, decoder with skip connections. Nonetheless, IRT-SIREN U-Net replaces the non-linearities in each convolutional block with sinusoidal activations defined as

$$\phi(x) = sin(w_0 x),$$

where $w_0 = 30$ is a frequency scaling factor that controls the periodicity of the activation function. Consequently, the complete transformation performed by each SIREN convolution block in Fig. 2b and 2c is expressed by

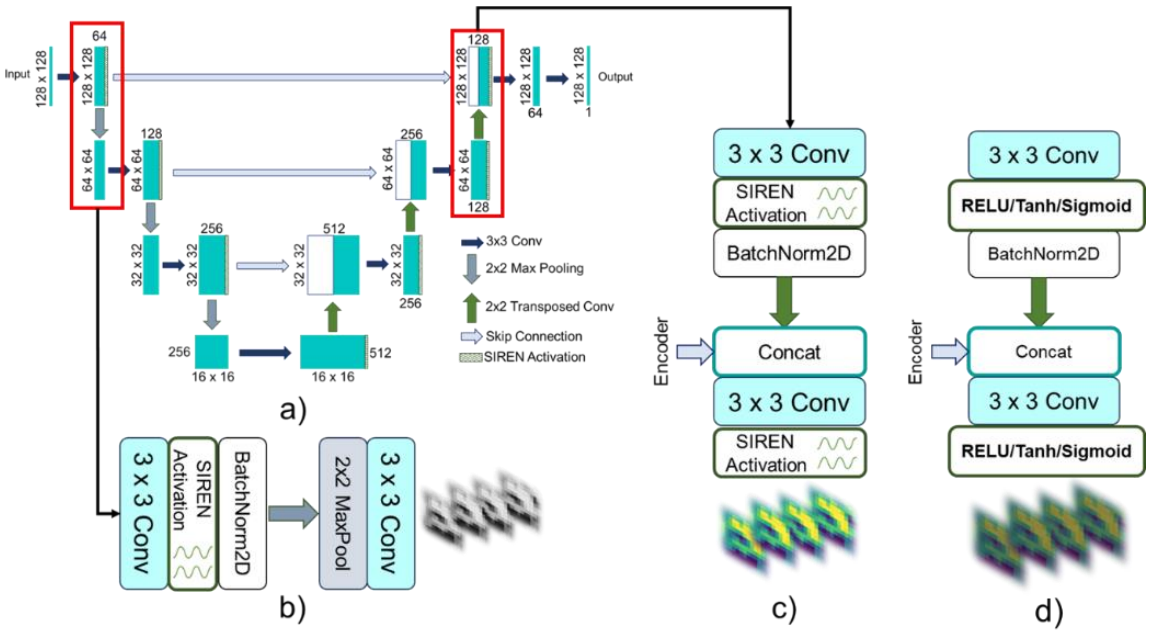

Fig. 2: a) IRT-SIREN U-Net architecture. b) and c) IRT-SIREN U-Net layers incorporating periodic activations. d) Traditional layers utilized in IRT U-Net with ReLU.

$$y_\ell' = \mathrm{BatchNorm2D}\big(\sin\big(\omega_0 \cdot (W_\ell * x_\ell + b_\ell)\big)\big).$$

In contrast, the traditional convolution block, see Fig. 2d, applies a non-periodic activation such as ReLU as

$$y_\ell = \mathrm{BatchNorm2D}\big(\beta(W_\ell * x_\ell + b_\ell)\big),$$

where $*$ denotes 2D convolution, β is a non-periodic activation function, x_ℓ is the input, W_ℓ are the weights, and b_ℓ is the bias of the ℓ-th layer, respectively. To ensure stable training and convergence with sine activations, the network's weights and biases must follow specific initialization criteria [26]. For instance, the weights of the first layer are initialized from a uniform distribution as

$$W_1 \sim \mathcal{U}\left(-\frac{1}{N_{\text{in}}}, \frac{1}{N_{\text{in}}}\right),$$

while for subsequent layers $\ell > 1$, the weights are initialized as

$$W_\ell \sim \mathcal{U}\left(-\sqrt{\frac{6}{N_{\text{in}}}}, \sqrt{\frac{6}{N_{\text{in}}}}\right).$$

After formulating the topology of IRT-SIREN U-Net, input thermographic representations are, PCA $\boldsymbol{P}$ and TSR $\mathbf{T}$, are fed to the network produce a segmentation mask, $M_i \in \{0,1,\dots,C-1\}^{N_y \times N_x}$, where C is the number of defect classes corresponding to the depth of the back-drilled hole. Max pooling and transposed convolutions are used for downsampling and upsampling, respectively, with skip connections preserving spatial features across consecutive resolution levels.

3.2. Implementation Details and Training

The proposed IRT-SIREN U-Net is implemented with a lightweight architecture comprising three encoder/deconvolutional blocks. Each convolution block integrates a 3×3 convolutional layer, sinusoidal activation, and batch normalization. Downsampling and upsampling are performed using 2×2 max pooling and transposed convolutions, respectively. On the other hand, IRT-SIREN U-Net is trained on the IRT-PVC on 26 inspection sequences randomly selected from the dataset and the network's accuracy is reported on the validation and testing datasets, each comprising of 6 randomly selected inspection samples. To improve generalization and reduce overfitting during training, data augmentation is applied, which incorporates random cropping, rotation, translation, and affine shearing.

Training is performed using a batch size of 8, with the Categorical Cross-Entropy (CCE) loss for multi-class segmentation defined as

$$\mathcal{L} = -\sum_{i=1}^{N}\sum_{c=1}^{C} y_{i,c}\log\big(\widehat{y_{i,c}}\big),$$

where N is the total number of samples within a batch, $y_{i,c}$ is the ground truth label, and $\widehat{y_{i,c}}$ is the predicted probability that pixel i belongs to class c. The network outputs a pixel-wise segmentation mask, $\boldsymbol{M_i} \in \{0,1,\dots,C-1\}^{N_y \times N_x}$, where C is the number of defect classes, including background. The model is optimized using the Adam optimizer with a learning rate of $1e-4$.

4. Results

4.1. Experimental Validation

The proposed framework is evaluated on the validation and testing datasets of the IRT-PVC dataset. Since multi-class segmentation is tackled, the evaluation metrics utilized are mean Intersection over Union (IoU), recall, and precision. Let TP_c, FP_c, FN_c denote denote the true positives, false positives, and false negatives for class c, and C be the total number of classes, the IoU for each class is computed as

$$\mathrm{IoU_c} = \frac{\mathrm{TP_c}}{\mathrm{TP_c} + \mathrm{FP_c} + \mathrm{FN_c}}.$$

Similarly, the recall and precision are evaluated by

$$\mathrm{Recall_c} = \frac{\mathrm{TP_c}}{\mathrm{TP_c} + \mathrm{FN_c}}, \mathrm{Precision_c} = \frac{\mathrm{TP_c}}{\mathrm{TP_c} + \mathrm{FP_c}}.$$

The metrics are reported on the validation and testing sets, where we also benchmark the IRT-SIREN U-Net against its traditional U-Net (e.g. ReLU) based on these metrics. It is worth mentioning that the reported metrics and benchmarks are reported for input representations TSR and PCA.

4.2. Defect Segmentation Evaluation

To assess the effectiveness of the proposed IRT-SIREN U-Net, its segmentation performance is evaluated when fed input representations, PCA and TSR. Two architectures are compared: the baseline U-Net and the proposed SIREN-based U-Net. This comparison enables a thorough evaluation of the influence of activation type on defect segmentation accuracy. Table 1 presents a qualitative comparison of the segmentation outputs for representative samples from the IRT-PVC test and validation sets. Ground truth defect masks are compared with predicted masks generated from PCA and TSR inputs processed by both the standard U-Net and IRT-SIREN U-Net. The SIREN-based model consistently produces sharper, more spatially coherent segmentations, particularly in detecting small or shallow defects that are often missed by the baseline U-Net. This improvement is especially evident when using PCA and TSR inputs, where the periodic activation better preserves thermal signal variations.

To quantify the two network accuracies, Table 2 provides segmentation performance in terms of mean IoU, recall, and precision. The proposed IRT-SIREN U-Net outperforms the baseline across all modalities, achieving the highest mIoU and recall scores. Notably, the largest performance gain is observed for the PCA input, with a 7% improvement in mIoU compared to the ReLU-based counterpart. This highlights the benefit of sinusoidal activations in extracting high-frequency features critical for detecting fine thermal anomalies. Collectively, the obtained results show that integrating sinusoidal activations into a U-Net backbone enhances the model's ability to leads to improved subsurface defect characterization.

5. Conclusions and Future Work

This paper presented the IRT-Sinusoidal Representation Network (IRT-SIREN U-Net), a modified U-Net architecture designed to enhance infrared thermography (IRT) defect segmentation through the use of periodic activation functions. Unlike conventional models that rely on ReLU, the proposed network incorporates sine activations to improve the network's ability to capture high-frequency thermal signal variations. Experimental results on the Université Laval IRT-PVC dataset demonstrate that IRT-SIREN U-Net achieves superior segmentation performance, with a 7% improvement in mean IoU compared to traditional activation-based models. This work highlights the significance of activation function choice in thermal defect analysis and opens new directions for leveraging implicit representations in AI-driven IRT.

Acknowledgments

This work was supported by Khalifa University of Science and Technology under Award 8474000660. The work was also supported by the Advanced Research and Innovation Center (ARIC), which is jointly funded by Aerospace Holding Company LLC, a wholly-owned subsidiary of Mubadala Investment Company PJSC and Khalifa University for Science and Technology.

Table 1: Qualitative comparisons between IRT-SIREN U-Net and traditional U-Net architecture for multi-class defect segmentation.

Input	Sample 1	Sample 2
U-Net PCA	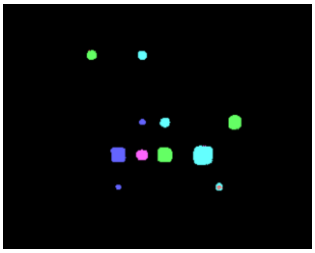	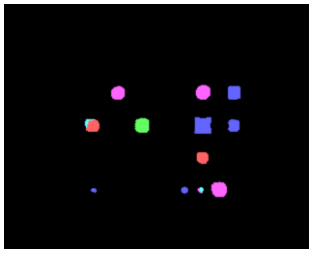
IRT-SIREN U-Net TSR	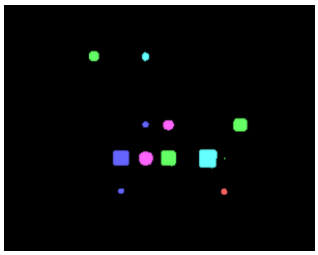	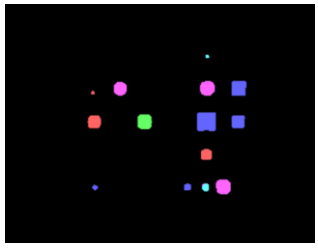
U-Net TSR	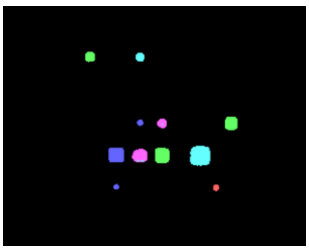	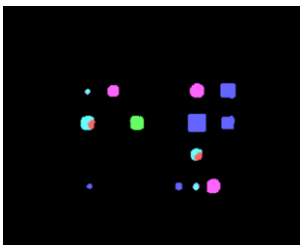
IRT-SIREN U-Net TSR	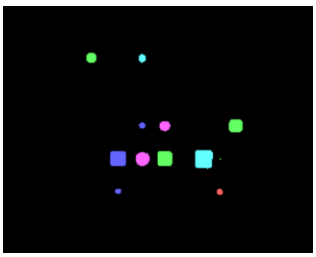	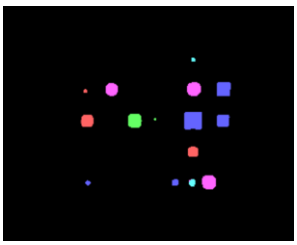
Ground Truth Mask	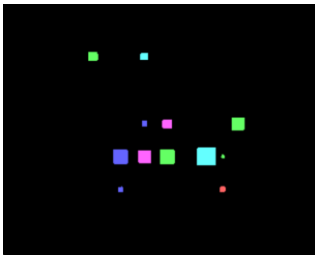	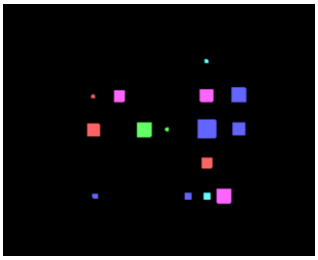

Table 2: Quantified segmentation performance of IRT-SIREN U-Net and traditional U-Net with ReLU activation.

Network	mIoU	Recall	Precision
PCA IRT-SIREN U-Net	0.811	0.804	0.811
PCA ReLU U-Net	0.724	0.756	0.732
TSR IRT-SIREN U-Net	0.824	0.827	0.836
TSR ReLU U-Net	0.747	0.773	0.782

REFERENCES

[1] M. Salah, A. Ayyad, M. Ramadan, Y. Abdulrahman, D. Swart, A. Abusafieh, L. Seneviratne and Y. Zweiri, "High speed neuromorphic vision-based inspection of countersinks in automated manufacturing processes," *J. Intell. Manuf.,* vol. 35, *(7),* pp. 3067–3081, 2024. . DOI: 10.1007/s10845-023-02187-0.

[2] M. E. Torbali, A. Zolotas and N. P. Avdelidis, "A State-of-the-Art Review of Non-Destructive Testing Image Fusion and Critical Insights on the Inspection of Aerospace Composites towards Sustainable Maintenance Repair Operations," *Applied Sciences,* vol. 13, *(4),* pp. 2732, 2023. . DOI: 10.3390/app13042732.

[3] Y. He, B. Deng, H. Wang, L. Cheng, K. Zhou, S. Cai and F. Ciampa, "Infrared machine vision and infrared thermography with deep learning: A review," *Infrared Phys. Technol.,* vol. 116, pp. 103754, 2021. . DOI: 10.1016/j.infrared.2021.103754.

[4] Z. Wei, A. Osman, B. Valeske and X. Maldague, "A Dataset of Pulsed Thermography for Automated Defect Depth Estimation," *Applied Sciences,* vol. 13, *(24),* pp. 13093, 2023. . DOI: 10.3390/app132413093.

[5] Z. Wei, A. Osman, B. Valeske and X. Maldague, "Pulsed Thermography Dataset for Training Deep Learning Models," *Applied Sciences,* vol. 13, *(5),* pp. 2901, 2023. . DOI: 10.3390/app13052901.

[6] Y. Dong, C. Xia, J. Yang, Y. Cao, Y. Cao and X. Li, "Spatio-Temporal 3-D Residual Networks for Simultaneous Detection and Depth Estimation of CFRP Subsurface Defects in Lock-In Thermography," *TII,* vol. 18, *(4),* pp. 2571–2581, 2022. . DOI: 10.1109/TII.2021.3103019.

[7] G. Zhou, Z. Zhang, W. Yin, H. Chen, L. Wang, D. Wang and H. Ma, "Surface defect detection of CFRP materials based on infrared thermography and Attention U-Net algorithm," *Nondestr. Test. Eval.,* vol. 39, *(2),* pp. 238–257, 2024. . DOI: 10.1080/10589759.2023.2191954.

[8] Y. A. Abdulrahman, M. A. Omar, Z. Said, F. Obeideli, A. Abusafieh and G. N. Sankaran, "A Taguchi Design of Experiment Approach to Pulse and Lock in Thermography, Applied to CFRP Composites," *J Nondestruct Eval,* vol. 36, *(4),* pp. 1–11, 2017. . DOI: 10.1007/s10921-017-0450-4.

[9] M. A. Omar, Z. Said, A. A. Raisi, Y. A. A. Rahman, A. Abusafieh and G. N. Sankaran, "The Calibration and Sensitivity Aspects of a Self-Referencing Routine When Applied to Composites Inspection: Using a Pulsed Thermographic Setup," *J Nondestruct Eval,* vol. 35, *(3),* pp. 1–10, 2016. . DOI: 10.1007/s10921-016-0367-3.

[10] N. N. Kulkarni, K. Raisi, N. A. Valente, J. Benoit, T. Yu and A. Sabato, "Deep learning augmented infrared thermography for unmanned aerial vehicles structural health monitoring of roadways," *Autom. Constr.,* vol. 148, pp. 104784, 2023. . DOI: 10.1016/j.autcon.2023.104784.

[11] J. Wang and T. Ueda, "A review study on unmanned aerial vehicle and mobile robot technologies on damage inspection of reinforced concrete structures," *Structural Concrete : Journal of the FIB,* vol. 24, *(1),* pp. 536–562, 2023. . DOI: 10.1002/suco.202200846.

[12] D. Roy, P. Babu and S. Tuli, "Sparse Reconstruction-Based Thermal Imaging for Defect Detection," *TIM,* vol. 68, *(11),* pp. 4550–4558, 2019. . DOI: 10.1109/TIM.2018.2889364.

[13] E. Candes, X. Li, Y. Ma and J. Wright, "Robust principal component analysis?: Recovering low-rank matrices from sparse errors," in 2010, pp. 201–204. DOI: 10.1109/SAM.2010.5606734.

[14] C. Wen, S. Sfarra, G. Gargiulo and Y. Yao, "Thermographic Data Analysis for Defect Detection by Imposing Spatial Connectivity and Sparsity Constraints in Principal Component Thermography," *TII,* vol. 17, *(6),* pp. 3901–3909, 2021. . DOI: 10.1109/TII.2020.3010273.

[15] A. Schager, G. Zauner, G. Mayr and P. Burgholzer, "Extension of the Thermographic Signal Reconstruction Technique for an Automated Segmentation and Depth Estimation of Subsurface Defects," *Journal of Imaging,* vol. 6, *(9),* pp. 96, 2020. . DOI: 10.3390/jimaging6090096.

[16] Z. Wei, H. Fernandes, H. Herrmann, J. R. Tarpani and A. Osman, "A Deep Learning Method for the Impact Damage Segmentation of Curve-Shaped CFRP Specimens Inspected by Infrared Thermography," *Sensors (Basel, Switzerland),* vol. 21, *(2),* pp. 395, 2021. . DOI: 10.3390/s21020395.

[17] S. He, S. Zhang, D. Mishra and M. M. Yuen, "A graph learning approach for automatic subsurface defects segmentation in building façade using RGB and infrared images," *E-Journal of Nondestructive Testing,* vol. 29, *(7),* 2024. . DOI: 10.58286/29567.

[18] M. Moradi, R. Ghorbani, S. Sfarra, D. M. J. Tax and D. Zarouchas, "A Spatiotemporal Deep Neural Network Useful for Defect Identification and Reconstruction of Artworks Using Infrared Thermography," *Sensors (Basel, Switzerland),* vol. 22, *(23),* pp. 9361, 2022. . DOI: 10.3390/s22239361.

[19] Z. Tong, L. Cheng, S. Xie and M. Kersemans, "A flexible deep learning framework for thermographic inspection of composites," *NDT & E International : Independent Nondestructive Testing and Evaluation,* vol. 139, pp. 102926, 2023. . DOI: 10.1016/j.ndteint.2023.102926.

[20] D. Müller, U. Netzelmann and B. Valeske, "Defect shape detection and defect reconstruction in active thermography by means of two-dimensional convolutional neural network as well as spatiotemporal convolutional LSTM network," *Quantitative Infrared Thermography,* vol. 19, *(2),* pp. 126–144, 2022. . DOI: 10.1080/17686733.2020.1810883.

[21] Q. Fang, C. Ibarra-Castanedo, I. Garrido, Y. Duan and X. Maldague, "Automatic Detection and Identification of Defects by Deep Learning Algorithms from Pulsed Thermography Data," *Sensors (Basel, Switzerland),* vol. 23, *(9),* pp. 4444, 2023. . DOI: 10.3390/s23094444.

[22] G. Zhou, Z. Zhang, W. Yin, H. Chen, L. Wang, D. Wang and H. Ma, "Surface defect detection of CFRP materials based on infrared thermography and Attention U-Net algorithm," *Nondestr. Test. Eval.,* vol. 39, *(2),* pp. 238–257, 2024. . DOI: 10.1080/10589759.2023.2191954.

[23] H. Yu, J. Wang, Z. Wang, J. Yang, K. Huang, G. Lu, F. Deng and Y. Zhou, "A lightweight network based on local–global feature fusion for real-time industrial invisible gas detection with infrared thermography," *Applied Soft Computing,* vol. 152, pp. 111138, 2024. . DOI: 10.1016/j.asoc.2023.111138.

[24] E. D'Accardi, F. Palano, R. Tamborrino, D. Palumbo, A. Tatì, R. Terzi and U. Galietti, "Pulsed Phase Thermography Approach for the Characterization of Delaminations in CFRP and Comparison to Phased Array Ultrasonic Testing," *J Nondestruct Eval,* vol. 38, *(1),* pp. 1–12, 2019. . DOI: 10.1007/s10921-019-0559-8.

[25] U. Netzelmann and D. Müller, "Modified pulse-phase thermography algorithms for improved contrast-to-noise ratio from pulse-excited thermographic sequences," *NDT & E International : Independent Nondestructive Testing and Evaluation,* vol. 116, pp. 102325, 2020. . DOI: 10.1016/j.ndteint.2020.102325.

[26] V. Sitzmann, J. N. P. Martel, A. W. Bergman, D. B. Lindell and G. Wetzstein, "Implicit Neural Representations with Periodic Activation Functions," *arXiv Cs.CV],* 2020. Available: http://arxiv.org/abs/2006.09661.